

THE THERMAL COMPOSITE SUPERNOVA REMNANT KES 27 AS VIEWED BY *CHANDRA*: SHOCK REFLECTION FROM A CAVITY WALLYANG CHEN¹, FREDERICK D. SEWARD², MING SUN³, JIANG-TAO LI¹,*Draft version November 2, 2018*

ABSTRACT

We present a spatially resolved spectroscopic study of the thermal composite supernova remnant Kes 27 with *Chandra*. The X-ray spectrum of Kes 27 is characterized by K lines from Mg, Si, S, Ar, and Ca. The X-ray emitting gas is found to be enriched in sulphur and calcium. The broadband and tri-color images show two incomplete shell-like features in the northeastern half and brightness fading with increasing radius in the southwest. There are over 30 unresolved sources within the remnant. None show characteristics typical of young neutron stars. The maximum diffuse X-ray intensity coincides with a radio bright region along the eastern border. In general, gas in the inner region is at higher temperature and emission is brighter than from the outer region. The gas in the remnant appears to approach ionization equilibrium. The overall morphology can be explained by the evolution of the remnant in an ambient medium with a density enhancement from west to east. We suggest that the remnant was born in a pre-existing cavity and that the inner bright emission is due to the reflection of the initial shock from the dense cavity wall. This scenario may provide a new candidate mechanism for the X-ray morphology of other thermal composite supernova remnants.

Subject headings: ISM: individual (Kes 27, G327.4+0.4) — radiation mechanism: thermal — supernova remnants — X-rays: ISM — shock waves

1. INTRODUCTION

Massive stars evolve rapidly and can explode not far from the dense clouds which were their birthplaces. The resulting supernova remnants (SNRs), then, are expected to be in the vicinity of, and to interact with, molecular and/or H I clouds. Such interaction may account for the characteristics of the thermal composite (or mixed-morphology) SNRs, which radiate bright thermal X-ray emission interior to their radio shells and have faint X-ray rims (Green et al. 1997; Rho and Petre 1998; Yusef-Zadeh et al. 2003). Several mechanisms have been proposed to interpret the X-ray morphology of the thermal composites. These mechanisms include (1) a radiatively cooled rim and a hot interior (e.g., Harrus et al. 1997; Rho & Petre 1998), (2) the hot interior with density increased due to thermal conduction (Cox et al. 1999; Shelton et al. 1999), (3) internal gas density increased due to evaporation of the engulfed cloudlets (White & Long 1991), and (4) shock interaction at the edge of a cloud but seen brightened in the projected interior (Petruk 2001; as summarized in, e.g., Chen et al. 2004). Recently, Shelton et al. (2004) have explained the X-ray properties of SNR W44 invoking thermal conduction and bright metal emission due to dust destruction and ejecta enrichment in the interior. Also, a study based on ionization states of hot interior plasma suggests that the thermal composite (or mixed-morphology) phenomenon may be an evolutionary state of SNRs as a result of thermal conduction (Kawasaki et al. 2005). The sample comprised six thermal composites including SNR Kes 27, which is

the subject of this paper.

In all of these mechanisms the influence of the supernova progenitor on the surrounding medium has not been considered. Massive stars may sculpt a cavity with their energetic stellar winds and ionizing radiation before they explode as core-collapse supernova. The observational effect of the blast wave of SNR impacting the cavity wall should be of particular interest. After almost free expansion in the cavity, the blast wave “reflects” from the cavity wall and a strong reverse shock heats the interior material. Thus a particular X-ray bright interior may be expected in this scenario, as we will outline for the case of Kes 27.

SNR Kesteven 27 (G327.4+0.4) is one of the archetypal thermal composites (Rho & Petre 1998; Enoguchi et al. 2002). Seen in X-rays with *Einstein* (Seward 1990), *ROSAT* (Seward et al. 1996), and *ASCA* (Enoguchi et al. 2002), it appeared prominently brightened in the center, especially along an inner broken ring. This is different from most of the other thermal composites that are centrally-peaked in X-rays. In the radio band (Kesteven & Caswell 1987; Whiteoak & Green 1996), there is a clear-cut rim except in the southwest (SW). The radio emission is brightest in the east, with the surface brightness peaked near the southeastern border, where the blast wave may be striking on a dense cloud. Radio emission gradually fades in the SW, where the remnant seems to break out to a lower density region. It was noted that the radio image also displays multiple arcs centered on the eastern half, from which a series of arc-like shells may have emanated (Milne et al. 1989).

Although no OH masers, which usually mark shock interaction with molecular clouds, are detected in Kes 27 (as in the cases of other thermal composites such as 3C 391, W28, and W44) (Green et al. 1997), this SNR is found to be embedded in a H I cloud complex at a

¹ Department of Astronomy, Nanjing University, Nanjing 210093, P.R.China

² Harvard-Smithsonian Center for Astrophysics, 60 Garden Street, Cambridge, MA 02138

³ Department of Physics and Astronomy, MSU, East Lansing, MI 48824

local standard rest velocity of 70 km s^{-1} . There is an H I ridge or shell just exterior to the rim, delineated by the radio continuum contours except on the western and southwestern sides (McClure-Griffiths et al. 2001). The authors suggest that this confirms that the remnant shock impacts a density enhancement for the inner void. The H I observation provides an estimate of dynamical distance $\sim 4.3 \text{ kpc}$, on the far side of the Scutum-Crux Arm. In this paper we will take this value as a reference for the distance: $d = 4.3 d_{4.3 \text{ kpc}}$.

Here we present a spatially-resolved X-ray spectroscopic study of the remnant using a *Chandra* ACIS-I observation. We briefly describe the observation and data calibration, and present our analysis and results in § 2. The physical properties of the thermal X-ray emission are discussed in § 3. We summarize our results in § 4. Statistical errors are all presented in the 90% confidence level.

2. OBSERVATIONS AND DATA ANALYSIS

SNR Kes 27 was observed with the Advanced CCD Imaging Spectrometer (ACIS) on board the *Chandra* X-ray observatory on 2003 June 21 (ObsID 3852) for 39 ks. The target center ($15^{\text{h}}48^{\text{m}}31^{\text{s}}.5$, $-53^{\circ}46'20''$) was placed for optimal coverage of the X-ray bright region of the remnant (see Fig. 1) on the four ACIS-I CCD chips. We reprocessed the event files (from Level 1 to Level 2) using the CIAO data processing software (version 3.2.2)⁴ to remove pixel randomization and to correct for CCD charge-transfer inefficiencies. After removing flares with count rates greater than 1.2 times the mean light curve value, a net exposure of 37 ks remained and was used for analysis.

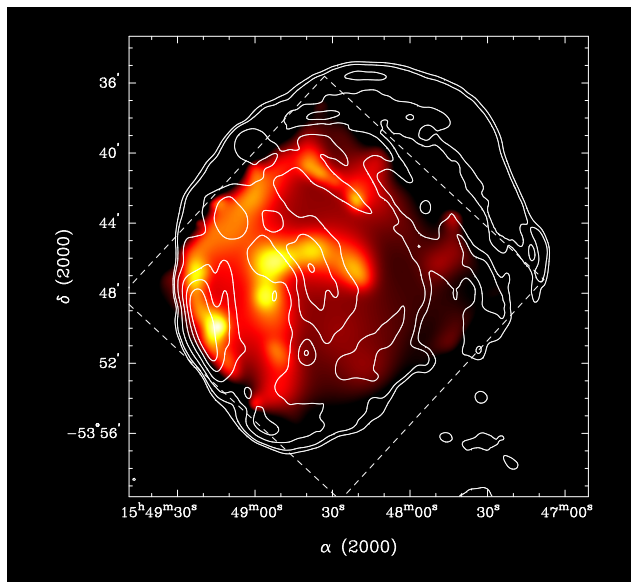


FIG. 1.— Broadband (0.3–7 keV) diffuse X-ray image (in square-root scales between 64 and $4.8 \times 10^2 \text{ photons cm}^{-2} \text{ s}^{-1} \text{ ster}^{-1}$) overlaid with MOST 843 MHz radio contours (at square-root scale levels 0.01, 0.02, 0.05, 0.10, 0.17, 0.25, and $0.36 \text{ Jy beam}^{-1}$) (from Whiteoak & Green 1996). The X-ray image is exposure-corrected and is adaptively smoothed to achieve a S/N ratio of 4 (using the CIAO program *csmooth*). The dashed box denotes the field of view of ACIS-I.

2.1. Source identification and optical counterparts

A major goal of this observation was to search for an internal compact object. There is obviously no bright Crab-like pulsar or pulsar wind nebula (PWN) within Kes 27. However, less energetic PSR/PWN examples have been observed in many other remnants, for example IC 443 (1.5 kpc distant) and in the Vela Remnant (0.25 kpc distant) (Olbert et al. 2001; Helfand et al. 2001). Upper limits can be set for these types of PWN.

If moved to the more distant Kes 27, the IC 443 PWN ($L_x = 3 \times 10^{33} \text{ ergs s}^{-1}$, $2' \times 1'$ in extent) would appear as a $0.7' \times 0.35'$ patch in the 2–8 keV X-ray band with strength $\approx 20 \text{ counts ks}^{-1}$. We can set an upper limit of 1 count ks^{-1} for an object of this size in the interior of Kes 27 so $L_x \leq 1.5 \times 10^{32} \text{ ergs s}^{-1}$. Similar reasoning for the Vela PWN ($1.6'$ in diameter, $L_x = 7 \times 10^{32} \text{ ergs s}^{-1}$) predicts 7 counts ks^{-1} from a $6''$ region. In this case we can set an upper limit of $0.5 \text{ counts ks}^{-1}$ corresponding to $L_x \leq 0.5 \times 10^{32} \text{ ergs s}^{-1}$. Note that an upper limit depends strongly on the size of the object. Leahy (2004) has suggested that the PSR/PWN within the IC 443 boundary is really associated with the nearer remnant G189.6+3.3. Although this would reduce its luminosity to $\approx 1/4$ that quoted above, our upper limit does not change.

The thermal composite remnant Kes 79 (7 kpc distant) contains an unresolved central compact object (CCO) with $L_x = 7 \times 10^{33} \text{ ergs s}^{-1}$ (Seward et al. 2003). The spectrum is soft, but since absorption is comparable in the two remnants, if this object were in Kes 27, we would expect $40 \text{ counts ks}^{-1}$, twice as bright as the brightest observed unresolved source. The hardness ratio (defined in Table 1 footnotes) should be ≈ 0.5 and no variation or optical counterpart is expected. As described below, we searched for such an object and did not find one. An upper limit of $0.8 \text{ counts ks}^{-1}$ yields $L_x \leq 1.4 \times 10^{32} \text{ ergs s}^{-1}$ for any CCO in Kes 27.

We first searched for point-like sources in the broad band (0.3–7.0 keV) with a wavelet source-detection algorithm. Thirty sources with a S/N ratio $\gtrsim 4$ in the field of view (the range of the four ACIS-I chips) are listed in Table 1, and identified in Figure 2. The spectrum of each source is characterized by a hardness ratio, defined in the table footnotes. This is useful in identifying red stars and AGN. The count rates listed were taken from *Chandra* automatic processing. Optical data were taken from the 2MASS catalog (2003) (J, H, K) and the USNO Catalog (2007) (B, R, I). If no cataloged source was within 1 arcsec of the X-ray position, no optical data are listed. Most Table 1 sources have soft X-ray spectra and optical counterparts with $0.0 < J - H < 0.8$, $0.0 < H - K < 0.4$. These are identified as stars and are probably spectral type K or M (Tokunga 1999). X-ray spectra of these clearly show less absorption than that of Kes 27 so these are clearly foreground objects – as well they should be. Sources 9 and 11, with harder spectra, are probably highly reddened stars. Even though not many photons were collected, the X-ray flux from some sources is quite variable. The approximate variation is listed.

⁴ <http://cxc.harvard.edu/ciao/>

TABLE 1
Chandra SOURCE LIST

Source (1)	CXOU Name (2)	CR (cts ks ⁻¹) (3)	HR (4)	<i>J</i> (5)	<i>H</i>	<i>K</i>	<i>B</i>	<i>R</i>	<i>I</i>	comment
1	J154722.45–534552.6	0.81±0.18	0.80±0.18	14.07	13.54	13.45	17.42	16.05	15.27	?
2	J154737.93–534639.6	2.55±0.29	-0.10±0.12	star?, varies
3	J154802.08–534549.3	1.53±0.23	-0.19±0.16	12.16	11.44	11.17	16.75	14.77	14.02	star
4	J154805.52–534050.5	0.75±0.17	-0.64±0.21	11.50	11.23	11.17	star
5	J154805.67–534018.7	0.67±0.16	-0.44±0.25	13.23	12.77	12.71	16.01	14.63	14.28	star
6	J154808.11–534128.1	1.07±0.20	-0.70±0.16	10.84	10.67	10.61	11.69	11.59	11.56	star
7	J154816.79–534125.5	7.03±0.46	0.95±0.03	AGN
8	J154817.90–535654.4	0.86±0.18	-0.44±0.21	13.30	11.66	10.81	15.58	14.26	13.99	star
9	J154819.85–534618.3	2.17±0.27	0.28±0.13	10.83	9.74	9.31	19.49	15.63	13.95	star
10	J154820.19–535447.9	1.05±0.20	-0.54±0.18	14.86	14.11	13.95	18.08	16.43	15.37	star
11	J154820.78–534222.4	1.07±0.20	0.15±0.20	14.01	13.04	12.65	20.61	18.54	17.11	star
12	J154822.10–535548.0	0.83±0.18	-0.29±0.22	12.88	12.34	12.21	16.02	14.64	14.05	star
13	J154826.38–534940.0	2.63±0.29	-0.37±0.11	13.42	12.70	12.47	17.56	14.87	14.28	star
14	J154829.60–534627.1	3.57±0.34	-0.53±0.09	13.24	12.66	12.44	star, flare x10
15	J154832.21–533736.3	1.80±0.25	0.64±0.12	AGN?
16	J154832.24–534028.0	0.97±0.19	0.89±0.14	AGN?
17	J154832.37–533916.8	57.55±1.27	-0.55±0.02	10.24	9.86	9.75	12.20	11.28	10.90	star, vary x2
18	J154832.96–535249.7	0.78±0.17	-0.52±0.22	20.02	18.70	16.68	star, vary x3
19	J154837.83–534955.7	2.47±0.29	-0.52±0.11	10.59	9.93	9.67	14.18	12.77	11.36	star
20	J154839.05–534316.1	0.72±0.17	-0.19±0.25	10.77	9.99	9.66	17.01	14.36	12.92	star
21	J154839.32–534527.1	0.97±0.19	-0.28±0.20	11.57	11.30	11.20	13.43	12.41	11.09	star
22	J154840.21–534043.6	13.20±0.62	-0.71±0.0	11.50	10.87	10.64	star, vary x3
23	J154840.68–534635.9	0.67±0.16	-0.44±0.25	12.52	12.16	12.08	14.57	14.06	13.69	star
24	J154841.14–534005.2	0.78±0.17	-0.03±0.24	13.74	13.22	13.01	17.27	15.55	14.91	star
25	J154842.55–535610.1	0.83±0.18	0.81±0.18	16.14	15.13	14.56	?
26	J154842.77–535213.4	0.83±0.18	-0.36±0.22	13.71	13.27	13.16	16.88	15.32	14.96	star
27	J154853.11–534806.2	1.50±0.23	-0.43±0.15	13.76	13.37	13.30	16.79	15.31	14.82	star
28	J154915.48–534407.8	1.34±0.22	0.72±0.14	15.91	14.97	14.34	?
29	J154916.18–534244.9	1.34±0.22	0.80±0.13	AGN?
30	J154932.56–535026.4	0.59±0.16	0.00±0.29	11.55	10.80	10.49	16.40	14.86	13.89	star

NOTE. — Column (1): Generic source number. (2): Chandra X-ray Observatory (unregistered) source name, following the Chandra naming convention and the IAU Recommendation for Nomenclature (e.g., <http://cdsweb.u-strasbg.fr/iau-spec.html>). (3): On-axis source broad-band count rate. (4): The hardness ratio defined as $HR = (\mathcal{H} - S)/(\mathcal{H} + S)$, where S and \mathcal{H} are the source count rates in the 0.3–1.5 and 1.5–7 keV bands, respectively. This table only lists sources with individual signal-to-noise ratios greater than 4 in the broad band ($S + \mathcal{H}$), with an exception for source 30, which has an S/N ratio of 3.8 but is obviously discernible in the tri-color image (Fig.3). (5): JHK from 2MASS Catalog (2003). BRI from USNO B1.0 Catalog (2007).

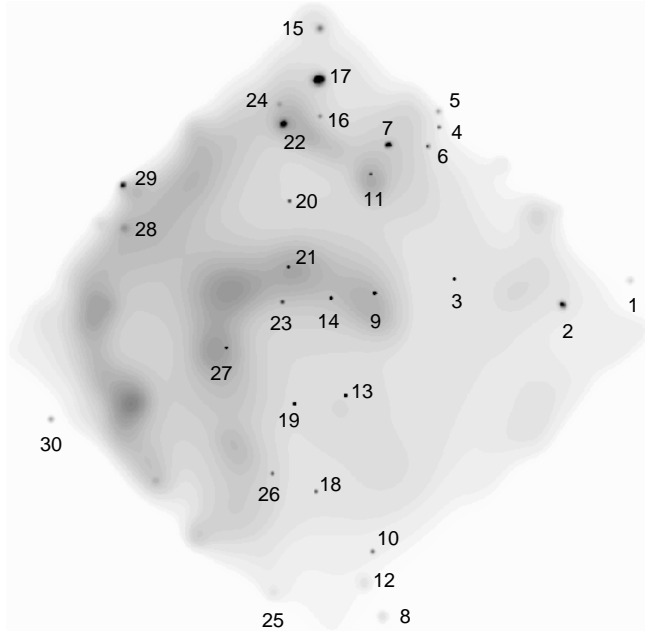


FIG. 2.— Identification of the unresolved sources listed in Table 1. This shows an adaptively smoothed 0.3–7 keV emission in logarithmic grayscale.

The bright source, 7, is quite hard, is strongly absorbed, and has no counterpart. This is probably a background AGN. Sources 15, 16, and 29 are also hard with no counterparts and likely to be AGN. The question mark (“?”) in Table 1 for these sources indicates classification based on hardness ratio. There were not enough events to determine a spectral shape. A typical AGN with strength of 1 count ks⁻¹ and with extinction corresponding to at least 2×10^{22} cm⁻², the column density in the path to Kes 27, will have hardness ratio ≥ 0.7 and $B \sim 27$, $R \sim 21$, and $H \sim 13$ (Seward 1999, NED 2007). There might be a counterpart in the infrared (J, H, K) but not in the optical bands (B, R). Sources 1, 25, and 28 are hard with apparent counterparts. Since these three are far from the focal point the X-ray location is not as accurate as for the more central sources and there is a higher probability that the counterparts listed are accidental. Sources 25 and 28, with IR counterparts only, could be AGN. Sources 2 and 18 are soft with no 2MASS counterpart. They are classified as stars because they were observed to vary.

The brightest unresolved source, 17, produces enough counts to derive spectral parameters. The spectrum can be best fitted with a thermal gas plus power-law model (see Fig.3). This source is weakly absorbed ($N_H \sim 6 \pm 4 \times 10^{20}$ cm⁻² s⁻¹), with powerlaw photon index $\Gamma \sim 2.9 \pm 0.2$, gas temperature $kT \sim 0.77_{-0.13}^{+0.07}$ keV,

probably overabundant Ne: $[\text{Ne}/\text{H}] \sim 3.4^{+3.0}_{-2.3}$, and an unabsorbed 0.5–10 keV flux $F_x \sim 5.9 \times 10^{-13} \text{ ergs cm}^{-2} \text{ s}^{-1}$ ($\chi^2/\text{d.o.f.} = 63.3/73$). The spectrum of the second brightest unresolved source, 22, can be fitted with a double thermal gas model ($N_{\text{H}} \sim 6 \pm 1 \times 10^{21} \text{ cm}^{-2}$, $kT_1 \sim 0.2^{+0.05}_{-0.02} \text{ keV}$, $kT_2 \sim 1.3^{+1.4}_{-0.6} \text{ keV}$, $F_x \sim 1.7 \times 10^{-12} \text{ ergs cm}^{-2} \text{ s}^{-1}$, $\chi^2/\text{d.o.f.} = 14.3/17$). These spectra and column densities are quite consistent with the identification as foreground stars.

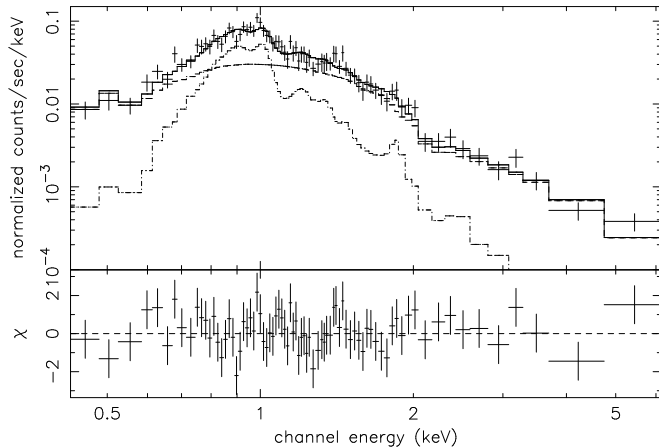


FIG. 3.— Spectrum of the northern hot spot (source 17), fitted with a *vmekal*+*power-law* model. The source spectrum is extracted from within a 3σ size, and the region of twice the 3σ size surrounding the source region is used as the background. The net count rate is $5.63 \pm 0.12 \times 10^{-2} \text{ cts/s}$. The spectrum has been adaptively binned to achieve a background-subtracted signal-to-noise ratio of 4.

Photons were sparse for most Table 1 sources. A few sources were not easy to classify. Source 2 is soft and has no optical counterpart but does not show enough interstellar absorption to be at the distance of the remnant. Source 15 has no counterpart and the hardness ratio is close to the 0.5 expected from a CCO. Since it is at the limb of the remnant, an AGN identification is more likely.

Two interior sources in the previous *ROSAT* image, 2 and 4, were identified as possible PSR/PWN candidates (Seward et al. 1996). These correspond respectively to *Chandra* sources 14 and 19 which are identified here as foreground stars.

2.2. Spatial Analysis

Fig. 1 presents the *Chandra* image of diffuse emission in the broad band (0.3 – 7.0 keV). Point sources were subtracted and the pixel values in source regions were replaced with values interpolated from the surrounding area. The X-ray image was then exposure-corrected and adaptively smoothed to achieve a S/N ratio of 4 (using the CIAO program *csmooth*). Contours of the MOST 843 MHz radio emission of the remnant (Whiteoak & Green 1996) are superposed on the X-ray image.

To demonstrate the energy dependence of the SNR morphology and the point sources, we also made a tri-color image in three energy bands: 0.3–1.5 keV (in red), 1.5–2.2 keV (in green), and 2.2–7.0 keV (in blue) as shown in Fig. 4. These three bands contain the Mg, Si, and S lines, which dominate the remnant’s thermal emission (see §2.3), respectively, and comparable pho-

ton fluxes. We first produced exposure maps in the three bands and used these for flat-fielding, accounting for bad-pixel removal, correcting for telescope vignetting, and correcting for quantum efficiency variation across the detector. The images in the three bands were then smoothed with an adaptive filter (using program *csmooth*) to achieve a broadband (0.3–7 keV) signal-to-noise ratio of 4.

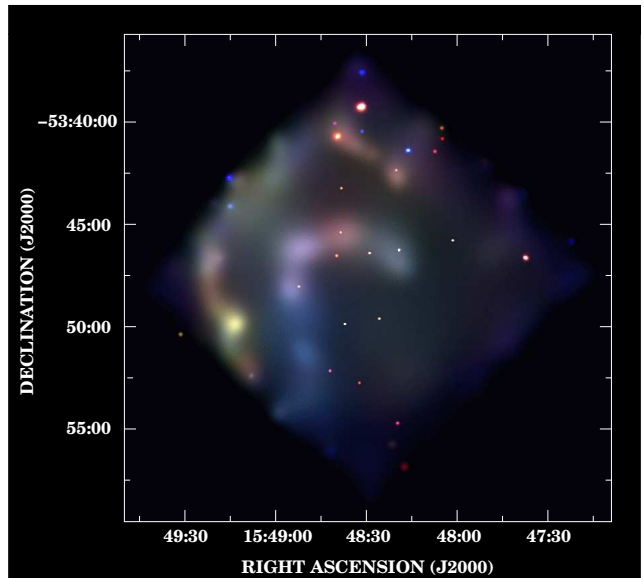


FIG. 4.— Tri-color ACIS-I image of Kes 27. The X-ray intensities in the 0.3–1.5, 1.5–2.2, and 2.2–7.0 keV bands are color coded in red, green, and blue, respectively, and are scaled logarithmically in ranges 19–170, 19–290, and 27–270 photons $\text{cm}^{-2} \text{ s}^{-1} \text{ ster}^{-1}$. The exposure-corrected X-ray maps were adaptively smoothed to achieve a broad-band (0.3–7 keV) S/N ratio of 4 (using the CIAO program *csmooth*).

Fig.1 and Fig.4 show that the X-ray emitting gas occupies a volume of linear size at least $17'$ (the size of the ACIS-I CCD chips) and the centroid of the X-ray emission lies in the eastern half of the remnant. The bright X-ray interior previously seen is now resolved into two semicircular arcs in the northeastern half of the remnant. The emission of the inner arc is harder than that of the outer arc (see Fig. 4). Apart from this bright, hard arc, there is an incomplete, soft arc along the northeastern outskirts. This outer arc is interior to the radio border. The X-ray surface brightness peaks near the southeastern border, where there is a bright X-ray knot (region E1 in Fig. 5) just inside the radio peak emission. This phenomenon is very similar to that on the western rim of SNR 3C391, where the blast wave has been suggested to propagate into a small dense region, causing drastic shock deceleration or the magnetic field compression and amplification (Chen et al. 2004). The soft, bright bar-like part of the outer arc in the north appears coincident with a radio arc (Fig. 1). The surface brightness radial profiles are plotted in Fig. 6. The two peaks in the northeast (NE) profile correspond to the two X-ray arcs, with mean radii of $2.5'$ and $6'$. The southwest profile shows that the X-ray emission fades with increasing radius and no shell-like structure can be discerned.

2.3. Spectral Analysis for the Diffuse Emission

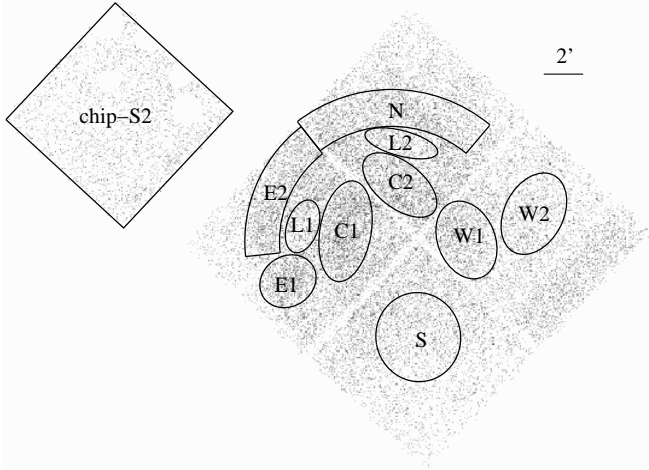


FIG. 5.— Raw image of the ACIS observation (with point-like sources removed). The labeled regions are used for spectrum extraction.

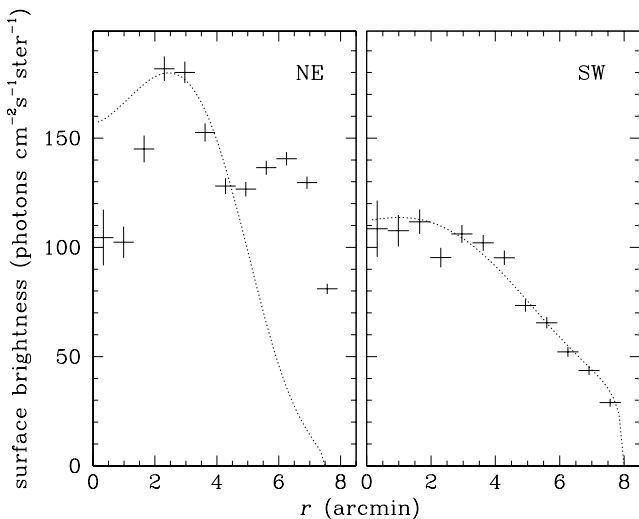


FIG. 6.— Exposure-corrected radial X-ray (0.3–7 keV) surface profiles for the NE and SW parts centered at RA=15^h48^m37^s.9, Dec.=−53°48′01″.9. The NE part is from position angle −46.8° to 133.2° and the SW part is from 133.2° to 313.2°. The blank sky exposure on the ACIS-I chips has been used for background. The dotted lines are plotted according to the White & Long (1991) model, relatively scaled to match the maximum brightness, with parameters $(\tau, C) = (10, 50)$ for the left panel and $(\tau, C) = (20, 56)$ for the right panel (see text).

After removal of point sources, we extracted the overall spectrum of diffuse emission from the whole area of the four ACIS-I CCD chips (excluding the peripheral edge) and other on-SNR spectra from 10 substructures marked in the raw-count image shown in Fig. 5. Because the field of view of the four ACIS-I chips is almost all covered by the remnant, a local background cannot be obtained from these chips, and hence a double background subtraction method was used. We extracted an off-SNR source-free spectrum from the ACIS-S2 chip (excluding the peripheral edge again, Fig. 5). The respective blanksky background⁵ contributions estimated from the

same regions and scaled by the flux at 9.5–12 keV⁶ were subtracted from the on- and off-SNR spectra. Individual on-SNR spectra were adaptively binned to achieve a background-subtracted signal-to-noise ratio of 4 and the off-SNR spectrum was binned using a ratio of 3. Each on-SNR spectrum was jointly fitted together with the off-SNR spectrum (Fig. 7). The on-SNR sky background is determined by scaling the off-SNR emission according to the region sizes (green lines in Fig. 7), which is phenomenally well described by a power-law with a photon index ~ 0.7 . Because of poor S/N ratio of the off-SNR spectrum below 1.2 keV, the counts below 1.2 keV in all the on-SNR spectra were ignored so as to match the off-SNR one. The XSPEC spectral fitting software (version 11.3)⁷ was used throughout. For the foreground absorption, the cross-sections of Morrison & McCammon (1983) were used and solar abundances assumed.

2.3.1. Overall Spectral Properties

The spectrum of the entire remnant (the left-upper panel of Fig. 7) shows distinct K α emission line features of metal elements: Mg XI (~ 1.34 keV), Si XIII (~ 1.84 keV), S XV (~ 2.43 keV), Ar XVII (~ 3.12 keV), and Ca XIX (~ 3.86 keV), confirming the thermal origin of the emission. We fit the net on-SNR spectrum with two absorbed non-equilibrium ionization (NEI) thermal plasma models, *vpshock* and *vsedov* (Borkowski, Lyerly, & Reynolds 2001; see Table 2). The former model characterizes the plasma parameters of a plane-parallel shock, typified by the constant electron temperature and the shock ionization timescale (the product of the electron density and the time since the passage of the shock). The latter is based on the Sedov (1959) dynamics, typified by the mean and the electron temperatures immediately behind the shock and the ionization timescale (the product of the electron density immediately behind the shock and the remnant's age). Because the NEI models do not include emission of argon, we added a Gaussian at 3.12 keV for the Ar line. Since this spectrum comprises contributions of various regions with different physical properties, it is not expected to be well fitted with a single thermal component model. However, it helps to sketch the overall properties of the hot gas interior to the remnant. The two models produce similar physical parameters but, by comparison of the statistical goodness, the *vsedov* model seems to better fit the spectrum than *vpshock*. Both models produce elevated abundances of S (~ 1.9 – 2.8 times solar) and Ca (~ 2.8 – 6.8), indicating that the plasma is metal enriched. The post-blast shock temperature $kT_s \sim 0.37$ – 0.51 keV derived with the *vsedov* model would correspond to a mean gas temperature $\approx 1.27kT_s \sim 0.47$ – 0.65 keV for the Sedov (1959) case, comparable to the mean temperature ~ 0.62 – 0.66 keV derived with the *vpshock* model. The mean ionization timescale is $\lesssim 10^{12} \text{ cm}^{-3} \text{ s}$ which indicates that the remnant as a whole is close to, but has not completely reached, ionization equilibrium. The unabsorbed fluxes (0.5–10 keV) in the field of view inferred from the two models are 2.3 – $2.7 \times 10^{-10} \text{ ergs cm}^{-2} \text{ s}^{-1}$

⁶ A high energy band free of sky emission, also see <http://cxc.harvard.edu/contrib/maxim/acisbg/>

⁷ <http://heasarc.gsfc.nasa.gov/docs/software/lheasoft/xanadu/xspec/xspec11/index.html>

⁵ <http://cxc.harvard.edu/contrib/maxim/acisbg/>, period-D

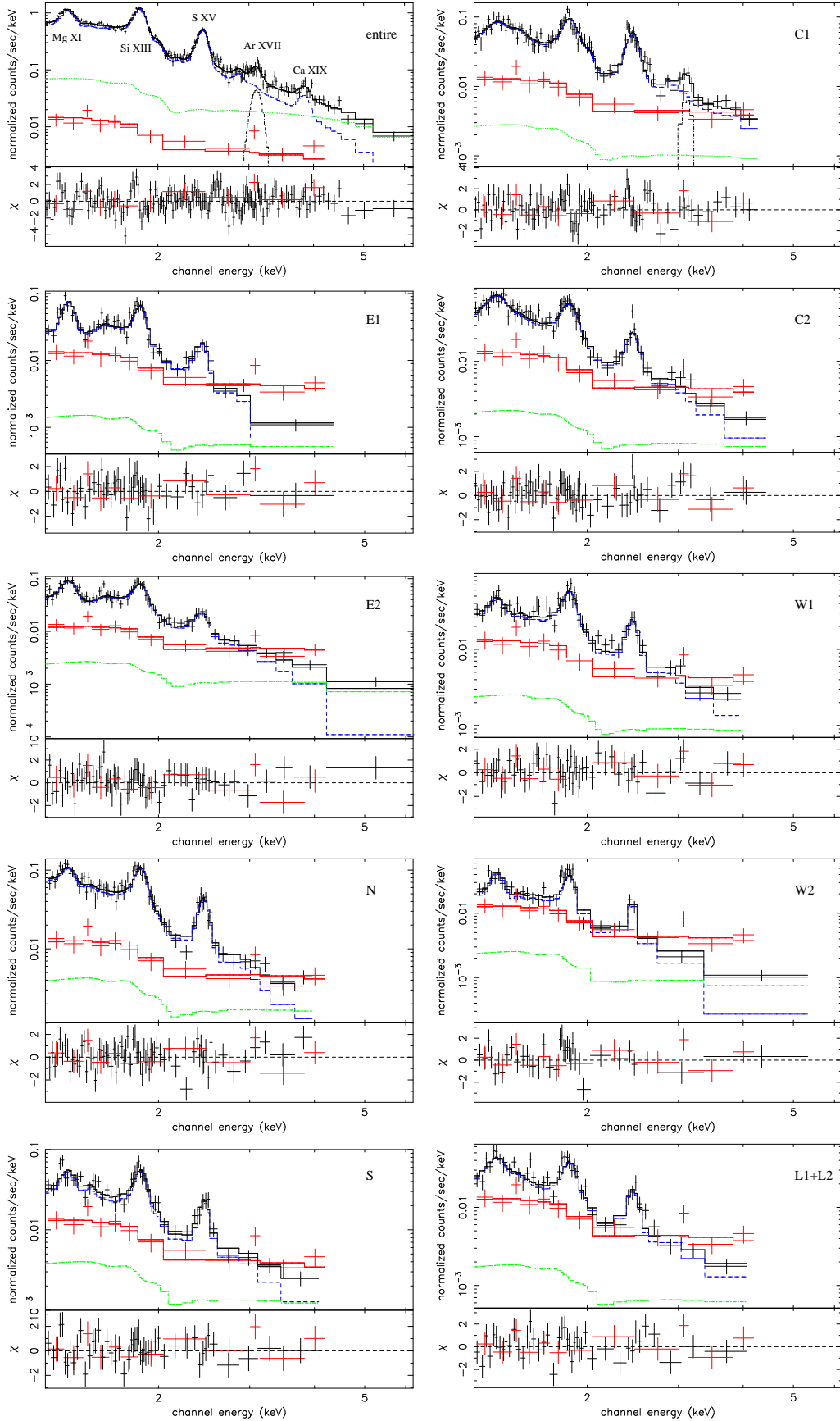


FIG. 7.— ACIS spectra of the entire remnant and the small regions shown in Fig.5. The on-SNR spectra (solid lines in black) were rebinned to achieve a background-subtracted S/N ratio of 4 and the off-SNR one (red) was rebinned using a ratio of 3. The net on-SNR spectra (blue) are fitted with an absorbed *vpshock* model, except for spectrum of the entire remnant for which an absorbed *vsedov* is used. The sky backgrounds (green) are scaled from the off-SNR spectrum, which is mimicked by a *power-law* model. The dot-dashed lines around 3.12 keV for the spectral fits of the entire remnant and region C1 are Gaussian accounting for the Ar XVII line.

and $5.4\text{--}8.6 \times 10^{-10} \text{ ergs cm}^{-2} \text{ s}^{-1}$, corresponding to an X-ray luminosity $5.1\text{--}6.0 \times 10^{35} d_{4.3}^2 \text{ ergs s}^{-1}$ and $1.2\text{--}1.9 \times 10^{36} d_{4.3}^2 \text{ ergs s}^{-1}$, respectively.

The spatial distribution of the relative strength of the S He α emission is shown in the equivalent width (EW) image of this line in Fig. 8. This image was constructed using a method similar to those used by Hwang et al. (2000) and Park et al. (2002). A major difference of our method from theirs is that we rebin the data using an adaptive mesh with each bin in each narrow band image including at least 10 counts (see Warren et al. 2003 for similar binning). The image shows that the S line emission is distributed over a broad region, but is strongest in the bright eastern portion of the inner arc. The Ca line is very weak and we have not produced a Ca EW image.

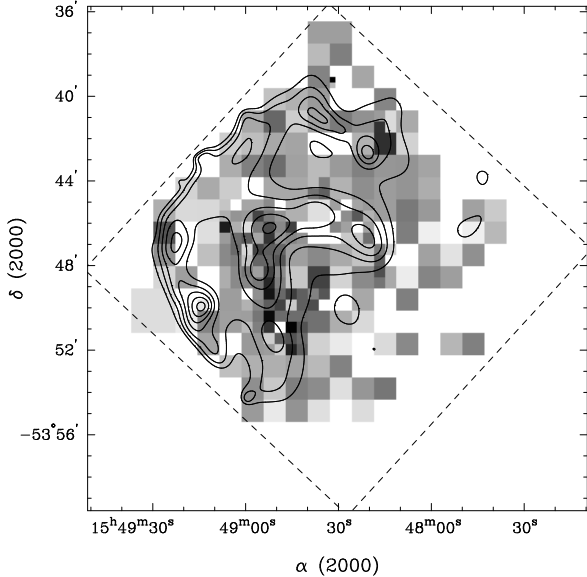


FIG. 8.— Equivalent width image of the S He α ($\sim 2.46 \text{ keV}$) line in square-root scale overlaid with the broadband (0.3–7 keV) diffuse X-ray contours (at seven logarithmic scale levels between $120\text{--}400 \text{ photons cm}^{-2} \text{ s}^{-1} \text{ ster}^{-1}$). The energy range used to extract the S line image was 2.28–2.70 keV, while the low- and high-energy ranges around the S line used to estimate the underlying continuum were 2.07–2.28 and 3.30–3.70 keV. The dashed box denotes the field of view of ACIS-I.

2.3.2. Small-scale Properties

The spectra of the 10 substructures all show distinct emission lines, indicating optically-thin thermal plasma. They were fitted with the *vpshock* model and spectral fit parameters are summarized in Table 3. A Gaussian at $\sim 3.1 \text{ keV}$ is added to account for the Ar XVII line in the region C1 spectrum. The model fits allow the abundances of key line elements to vary, while leaving other abundances fixed to the solar value. Estimates of the hydrogen number densities (n_H) inferred from the volume emission measures ($f n_e n_H V$, where f is the filling factor of the hot gas and $n_e \sim 1.2 n_H$ is assumed) are also given in Table 3 (and Table 2 for the entire remnant). In the derivation of the densities we have assumed that the 3-D shapes of the elliptical regions (E1,

C1, C2, W1, W2, S, L1, and L2) are ellipsoids, those of the arc-like regions (E2 and N) are projections of sphere segments, and that of the entire X-ray emitting volume is a sphere of diameter $17'$. Deviations from these assumptions and the non-uniformity of the X-ray-emitting plasma are consolidated into factor f of the individual regions. The regions show significant spectral variation. The gas temperatures ($\sim 1 \text{ keV}$) along the inner semicircular arc (regions C1 and C2) are higher than those ($\sim 0.4\text{--}0.7 \text{ keV}$) along the softer outer X-ray arc (regions E1, E2, and N). The densest gas in the eastern region E1 is consistent with the suggestion, based on the radio and X-ray brightness peaks, that the forward shock encounters a small dense region there (§2.2). The gas density of the low surface brightness regions (L1 and L2) between the two arcs is lower than in the two bright arcs. The ionization timescales for the small-scale regions (except E1 and E2) are around $10^{12} \text{ cm}^{-3} \text{ s}$ or even higher and hence they may be close to the ionization equilibrium; but the ionization timescales for the regions E1 and E2 (along the eastern outer shell) are relatively low ($0.6\text{--}3.0 \times 10^{11} \text{ cm}^{-3} \text{ s}$), indicating the plasma is far from ionization equilibrium. The sulphur abundance in most of the small-scale regions except E2 is somewhat higher than solar and seems to peak in region C1, the eastern portion of the inner arc, as shown in the S He α line distribution in the EW map.

3. DISCUSSION

The Kes 27 SNR has been classified as a thermal composite (or mixed-morphology) remnant. It is unusual in that the diffuse thermal X-ray emission does not peak in the center, but along two concentric semicircular arcs. The centroid of the X-ray emission lies in the eastern half of the remnant and the emission of the inner arc is harder than that of the outer region.

The thermal properties of Kes 27, as inferred from § 2.3, suggest that the X-ray emitting gas is essentially close to equilibrium of ionization (except for that along the eastern rim) and enriched with sulphur and calcium. If we adopt $n_H \sim 0.4 f^{-1/2} d_{4.3}^{-1/2} \text{ cm}^{-3}$ as the mean gas density, the mass of hot gas is $M = 1.4 n_H m_H f V \sim 110 f^{1/2} d_{4.3}^{5/2} D_{20}^3 M_\odot$, where m_H is the hydrogen atom mass and D_{20} is the remnant's diameter D scaled with the radio size $\sim 20'$ (thus $D \approx 25 D_{20} d_{4.3} \text{ pc}$). The thermal energy contained in the remnant is $E_{th} = (3/2) 2.3 n_H k T f V \sim 3 \times 10^{50} f^{1/2} d_{4.3}^{5/2} D_{20}^3 \text{ ergs}$, where mean temperature $kT \sim 0.6 \text{ keV}$ for the hot gas is used. With the shock temperature $kT_s \sim 0.4 \text{ keV}$, the shock velocity would be $v_s = (16 k T_s / 3 \bar{\mu} m_H)^{1/2} \sim 580 \text{ km s}^{-1}$, where the mean atomic weight $\bar{\mu} = 0.61$. The dynamical age of the remnant $\sim D / 5 v_s \sim 8.4 \times 10^3 d_{4.3} D_{20} \text{ yr}$ is derived with the Sedov (1959) solution which, because of the unusual morphology and complicated gas components, is only an approximation. The age estimate ($\sim 3.5 \times 10^3 \text{ yr}$) based on the *ROSAT* X-ray observation used a gas temperature (3.2 keV) which was too high (Seward et al. 1996). The Sedov model fit yields an ionization timescale $\tau_{\text{Sedov}} \sim 4.2 \times 10^{11} \text{ cm}^{-3} \text{ s}^{-1}$, which implies a dynamical age $t \approx \tau_{\text{Sedov}} / (1.2 \times 4 n_H) \sim 7 \times 10^3 f^{1/2} d_{4.3}^{1/2} \text{ yr}$

TABLE 2
SPECTRAL FITTING RESULTS FOR THE ENTIRE REMNANT WITH 90%
CONFIDENCE RANGES AND ESTIMATES OF THE GAS DENSITY

Models	<i>vpshock</i>	<i>vsedov</i>
χ^2_ν (d.o.f.)	1.89 (162)	1.57 (161)
N_H (10^{22} cm $^{-2}$)	2.3 ± 0.1	2.3 ± 0.1
Temperature (keV)	$kT_x = 0.63^{+0.03}_{-0.01}$ ^a	$kT_s = 0.41^{+0.10}_{-0.04}$ ^b $kT_e = 0.41^{+0.04}_{-0.03}$ ^b
Ion. Timescale (10^{11} cm $^{-3}$ s) ^c	$12.0^{+2.7}_{-4.8}$	$4.19^{+1.15}_{-0.83}$
$fn_e n_H V/d_{4.3}^2$ (10^{58} cm $^{-3}$) ^d	$2.01^{+0.10}_{-0.19}$	$3.36^{+0.85}_{-0.72}$
[Mg/H]	$0.85^{+0.09}_{-0.08}$	$0.63^{+0.08}_{-0.07}$
[Si/H]	$1.00^{+0.07}_{-0.06}$	$1.13^{+0.12}_{-0.09}$
[S/H]	$2.10^{+0.20}_{-0.22}$	$2.47^{+0.36}_{-0.28}$
[Ca/H]	$4.87^{+1.92}_{-1.77}$	$4.45^{+1.84}_{-1.66}$
Flux (10^{-10} ergs cm $^{-2}$ s $^{-1}$)	$2.56^{+0.12}_{-0.25}$	$6.88^{+1.74}_{-1.47}$
$n_H/f^{-1/2}d_{4.3}^{-1/2}$ (cm $^{-3}$) ^e	$0.34^{+0.01}_{-0.02}$	$0.44^{+0.06}_{-0.05}$

NOTE. — The unabsorbed fluxes are in the 0.5–10 keV band. The net count rates of the on- and off-source spectra are $8.52 \pm 0.06 \times 10^{-1}$ cts s $^{-1}$ and $1.86 \pm 0.14 \times 10^{-2}$ cts s $^{-1}$, respectively.

^a Mean electron temperature.

^b Mean shock temperature and electron temperature immediately behind the shock front, respectively.

^c The ionization timescale is defined as the product of the electron density and the time since the passage of the shock in the *vpshock* model, while as the product of the electron density immediately behind the shock and the remnant's age in the *vsedov* model. The value listed for *vpshock* is the upper limit for the range of the timescale.

^d f denotes the filling factor of the hot gas.

^e In the estimate of the densities, we assume a spherical volume of diameter $17'$ for the X-ray emitting gas.

TABLE 3
vpshock FITTING RESULTS WITH 90% CONFIDENCE RANGES AND ESTIMATES OF THE GAS DENSITY

regions	net count rate (10^{-2} cts s $^{-1}$)	χ^2_ν (d.o.f.)	N_H (10^{22} cm $^{-2}$)	kT_x (keV)	$n_e t$ (10^{11} cm $^{-3}$ s)	$fn_e n_H V/d_{4.3}^2$ ^a (10^{56} cm $^{-3}$)	[Mg/H]	[Si/H]	[S/H]	$n_H/f^{-1/2}d_{4.3}^{-1/2}$ (cm $^{-3}$)
E1	4.00 ± 0.11	1.07 (54)	2.7 ± 0.2	0.47 ± 0.04	$1.68^{+1.36}_{-0.42}$	$36.2^{+14.3}_{-11.1}$	$0.74^{+0.28}_{-0.20}$	$0.86^{+0.25}_{-0.19}$	$1.86^{+0.82}_{-0.63}$	$2.1^{+0.4}_{-0.3}$
E2	6.05 ± 0.14	0.92 (69)	$2.5^{+0.1}_{-0.2}$	$0.60^{+0.07}_{-0.06}$	$0.89^{+0.76}_{-0.34}$	$29.1^{+10.2}_{-4.6}$	$0.68^{+0.22}_{-0.17}$	$0.74^{+0.21}_{-0.08}$	$1.29^{+0.52}_{-0.45}$	$0.73^{+0.1}_{-0.0}$
N	7.58 ± 0.15	1.02 (75)	1.9 ± 0.2	$0.60^{+0.04}_{-0.02}$	$18.9 (> 5.6)$	$16.7^{+3.4}_{-4.2}$	$0.67^{+0.14}_{-0.21}$	$1.06^{+0.27}_{-0.22}$	$2.48^{+0.94}_{-0.66}$	$0.43^{+0.0}_{-0.0}$
S	4.18 ± 0.12	0.98 (54)	2.3 ± 0.2	$0.72^{+0.07}_{-0.05}$	$12.7 (> 3.8)$	$7.2^{+1.9}_{-1.0}$	1 ^c	1 ^c	$1.73^{+0.73}_{-0.55}$	$0.25^{+0.0}_{-0.0}$
C1	8.19 ± 0.16	1.26 (90)	1.8 ± 0.6	$1.21^{+0.45}_{-0.39}$	$3.7^{+22.6}_{-5.0}$	$4.7^{+6.2}_{-1.3}$	$0.83^{+0.52}_{-0.38}$	$1.44^{+0.43}_{-0.32}$	$2.97^{+0.39}_{-0.55}$	$0.43^{+0.2}_{-0.0}$
C2	5.13 ± 0.13	0.85 (68)	$2.1^{+0.2}_{-0.3}$	$0.76^{+0.25}_{-0.09}$	$7.2^{+31.8}_{-5.0}$	$6.7^{+2.4}_{-2.0}$	$1.22^{+0.45}_{-0.47}$	$1.10^{+0.40}_{-0.28}$	$1.92^{+0.88}_{-0.59}$	$0.63^{+0.1}_{-0.0}$
W1	4.12 ± 0.11	1.00 (54)	$2.6^{+0.3}_{-0.2}$	$0.69^{+0.05}_{-0.04}$	$7.6^{+72.2}_{-5.2}$	9.8 ± 2.7	$0.84^{+0.47}_{-0.40}$	$1.05^{+0.38}_{-0.29}$	$1.79^{+0.78}_{-0.56}$	0.37 ± 0.0
W2	2.73 ± 0.10	1.15 (39)	$2.3^{+0.3}_{-0.4}$	$0.62^{+0.05}_{-0.07}$	$7.3 (> 2.0)$	$6.7^{+3.8}_{-2.0}$	1 ^c	1 ^c	$1.92^{+1.15}_{-0.81}$	$0.30^{+0.0}_{-0.0}$
L1+L2	3.21 ± 0.10	1.17 (47)	$2.2^{+0.2}_{-0.3}$	0.89 ± 0.06	$5.2^{+13.6}_{-2.8}$	3.9 ± 1.3	1 ^c	1 ^c	$1.60^{+0.60}_{-0.54}$	0.26 ± 0.0

NOTE. — The net count rates of the on-source spectra are listed in the second column and that of off-source spectrum is $1.86 \pm 0.14 \times 10^{-2}$ cts s $^{-1}$.

^a f denotes the filling factor of the hot gas.

^b In the estimate of the densities, we assume oblate spheroids for elliptical regions E1 (with half-axes $1.50' \times 1.50' \times 1.29'$), C1 ($2.62' \times 2.62' \times 1.31'$), C2 ($2.22' \times 2.22' \times 1.18'$), ellipsoids (with half line-of-sight size the outer radius of shell region N $8'$) for regions W1 ($2.11' \times 1.49' \times 8'$), W2 (with half-axes $2.22' \times 1.50' \times 8'$), S ($2.34' \times 2.20' \times 8'$), L1 ($1.43' \times 0.82' \times 8'$), and L2 ($1.87' \times 0.84' \times 8'$), and sphere segments for regions E2 (with inner and outer radii of $7.6'$ and sector angle 80°) and N ($5.8'$, $8.0'$, 85°).

^c Fixed to the solar abundance.

(where we have assumed that the preshock density is similar to the mean interior density n_H). This is similar to the above Sedov age. On the other hand, the upper limit of the mean ionization timescale derived with *vpshock* model (Table 2) gives an age $\sim 9 \times 10^4 f^{1/2} d_{4.3}^{1/2}$ yr. It is similar to the ionization age ($> 8 \times 10^4$ yr) found in the ASCA X-ray study (Enoguchi et al. 2002) and is comparable to the remnant's radiative cooling timescale $t_{\text{cool}} \sim 4 \times 10^4 E_{51}^{0.24} (n_0/0.4 \text{ cm}^{-3})^{-0.52}$ yr, where E_{51} is

the SNR's explosion energy in units of 10^{51} ergs and n_0 is the preshock density (Falle 1981). In this case the post-shock temperature would be $\lesssim 1 \times 10^6$ K and thus the gas would be X-ray faint. This does not agree with the post-shock temperatures derived from the spectral fits and the fact that the eastern rim of the SNR is X-ray bright. A possibility for reconciling the different estimates could be that the X-ray emitting gas has a very low filling factor $f \lesssim 1 \times 10^{-2} D_{20}^2 d_{4.3}$ but this seems unlikely.

The mass of the X-ray emitting gas $\sim 10^2 f^{1/2} M_\odot$, sug-

gests that the SNR is not in the free expansion phase and is probably dominated by the swept-up ambient medium. Even so, Kes 27 appears to be S and Ca enriched and this is not a unique case. A sample of 23 thermal composite (or mixed-morphology) SNRs show that 10 of them are detected to be metal enhanced (Lazendic & Slane 2006). The contribution of SN ejecta has been suggested to be the cause of both the elevated metal abundances and the X-ray brightening in the central regions. For example, the overabundant Mg, Si, and (possibly) S in thermal composite SNR G290.1–0.8 (Slane et al. 2002) and the Ne, Si, and S enhancement in W44 are ascribed to SN ejecta (Shelton et al. 2004).

Nonuniform density environments are often seen around SNRs, especially those adjacent to dense clouds. This sometimes is consistent with systematic variation of the intervening hydrogen column density along the line of sight to SNRs, such as 3C391 (Chen et al. 2004) and 3C397 (Safi-Harb et al. 2005). The HI density enhancement is found to the east of the remnant (McClure-Griffiths et al. 2001) and the Spitzer IRAC $8\mu\text{m}$ observation (Reach et al. 2006) shows a large-scale environment around the Kes 27 SNR with a density gradient increasing from west to east. However, our X-ray study of Kes 27 does not show a clear trend for N_{H} (and spectral) variations along with the density gradient (although E1 is the only region showing a significantly higher value; Table 3). This may indicate that the environmental hydrogen column density may take only a very low fraction in the intervening interstellar column ($\sim 2 \times 10^{22} \text{ cm}^{-2}$), either because the cloud complex in the vicinity is not very compact or its size is not very large.

The double X-ray rings are not expected by either of the cloud evaporation and thermal conduction models. In the thermal conduction model (Cox et al. 1999; Shelton et al. 1999), thermal conduction in the remnant smooths out the temperature gradient from the hot interior to the cooler shell and increase the central density, resulting in luminous X-rays in the interior; this effect is dominant in the radiative stage. This model predicts a centrally-peaked X-ray surface brightness for the SNR, and a usually high ionization timescale for the hot gas, inconsistent with our observation. The cloud evaporation model (White & Long 1991) suggests that, when an SNR expands in an inhomogeneous interstellar medium whose mass is mostly contained in small clouds, the clouds engulfed by the blast wave can be evaporated to slowly increase the density of the interior hot gas; as a result, the SNR appears internally X-ray brightened. This model can reproduce an X-ray-bright inner ring like that in the NE half of Kes 27, and can also reproduce the fading-out radial surface brightness profile like that for the SW half (see Fig. 6). A representative fit to the inner ring brightness profile using the cloud evaporation model would need the ratio of the cloud evaporation timescale to the SNR's age $\tau = 10$ and the ratio of the mass of the cloudlets to the mass of the intercloud medium $C = 50$. The fit is not unique and combinations of $\tau = 8\text{--}12$ and $C = 40\text{--}60$ produce similar profiles (relatively scaled to match the maximum brightness). A representative fit to the SW radial brightness profile would need $\tau = 20$ (15–25) and $C = 56$ (45–70). However, the generally higher inner gas temperature than the outer region is not expected for such high τ and C values in the evaporation

model. Moreover, this model overestimates the surface brightness inside the inner ring and cannot reproduce the outer X-ray ring in the NE. It also cannot naturally explain why the physical conditions exemplified by parameters τ and C should be different in the two halves and why there are not two rings in the SW half as contrasted to the NE.

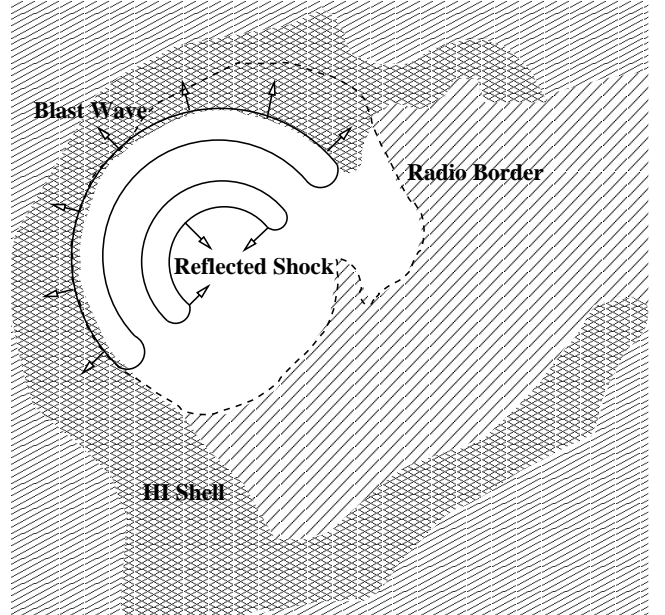


FIG. 9.— Diagram showing the structure and environment of the Kes 27 remnant.

Another scenario is required to account for the unusual X-ray morphology of Kes 27, which is different from those of other thermal composite remnants. Actually, the explanation must be consistent with the following facts: (1) The large-scale environment around the Kes 27 SNR has a density gradient increasing from west to east, as revealed in infrared (Reach et al. 2006). (2) As sketched in Fig. 9, the remnant is surrounded by a crocodile's mouth-like H I shell (McClure-Griffiths et al. 2001). (3) In X-rays, the remnant is brightened in the NE half and fades out to the SW low-density region. (4) The inner and outer X-ray arcs are both located in the NE half, where the ambient medium is denser than in the SW. (5) The outer arc is in contact with the H I shell. (6) The inner arc is hotter than the outer. (7) As noted by Enoguchi et al. (2002), the polarization of radio emission given by Milne et al. (1989) is strong in both the eastern rim and the center.

We suggest that both the outer and inner arcs represent shock waves, which propagate outward and inward, respectively. The observed polarization in the eastern rim and the center is due to shocked and compressed matter in the two arcs. The present inward shock is not the initial reverse shock due to expansion into low-density circumstellar material. The remnant is middle aged and this has long passed (McKee 1974). The present inward shock is a reverse shock due to the distant HI shell.

A comprehensive scenario is described in the following.

The massive progenitor exploded in a cavity excavated by the strong stellar wind and ionizing radiation. Because of the density gradient in the environmental medium, the wind-cavity has a small radius in the east and a large radius in the west or may even be not confined in the west. After the supernova explosion, in the west and SW, the blast wave propagated into a low-density medium and X-ray emission is faint. In the north and east, the blast wave has hit the cavity wall. A transmitted shock is now propagating into the dense wall and a reflected shock is traveling back toward the remnant center, shocking the SN ejecta to higher temperature. The outer arc contains gas heated by the transmitted shock and the inner arc is the interior metal-enriched gas heated by the reflected shock (see again Fig.9). Shock heated S atoms in the compressed inner arc emit a strong He α line.

Using the theory of reflected shocks described by Sgro (1975), we can estimate values for some parameters. For a shock reflected by a dense wall, the temperature ratio between the postreflected shock gas and posttransmitted shock gas is given by

$$\frac{T_r}{T_t} = \frac{A}{A_r}, \quad (1)$$

where A_r is the density contrast between the postreflected shock gas and postincident shock gas and A is the wall-to-cavity density contrast, which is related to A_r as

$$A = \frac{3A_r(4A_r - 1)}{\{[3A_r(4 - A_r)]^{1/2} - \sqrt{5}(A_r - 1)\}^2}. \quad (2)$$

The pressure ratio of the posttransmitted shock gas to the postincident shock gas is

$$\beta = \frac{4A_r - 1}{4 - A_r}. \quad (3)$$

Using these equations, we plot the functional relations of T_r/T_t , A_r , and β with A in Fig.10. Regions E2 vs. C1 and N vs. C2 represent two pairs of transmitted vs. reflected shocks. The ranges of the temperature ratios obtained from Table 3 are shown in Fig.10. Because there is a large scatter of the fitted temperatures, there are large uncertainties in the wall-to-cavity density A , which seems to be ~ 2 . The density contrast between the postreflected shock gas and postincident shock gas A_r is around 1.3. If regions W1, W2 and S can be roughly indicative of an postincident shock gas density $\sim 0.2-0.4f^{1/2}d_{4.3}^{1/2}\text{ cm}^{-3}$ (Table 3), then the postreflected shock density $0.4-0.6f^{1/2}d_{4.3}^{1/2}\text{ cm}^{-3}$ in C1 and C2 is consistent with the A_r values (but this estimate is crude because the filling factor f may vary from region to region).

Such a reflected shock launched from the cavity wall is consistent with the observational properties of SNR Kes 27. As the remnant ages, the transmitted shock in the dense medium will become fainter in X-rays while the reflected shock will converge in the center, producing a truly centrally X-ray brightened morphology. The reflection of shocks is thus another mechanism which may produce thermal composite remnants.

4. SUMMARY

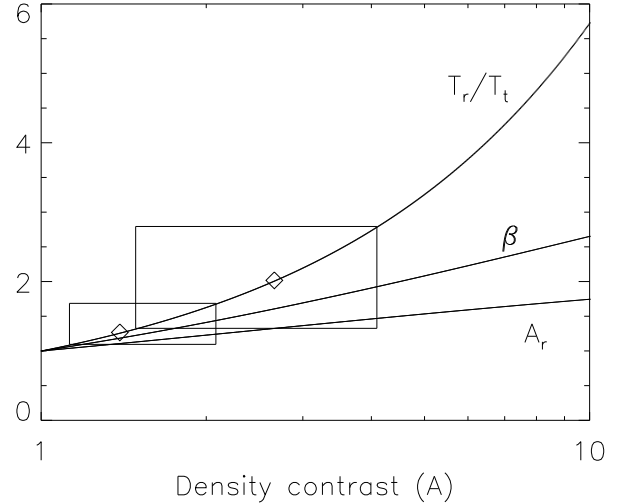


FIG. 10.— Parameters for the reflected shock. The large box represents the value ranges for region pair E2 and C1, and the small box is for region pair N and C2 (see text).

We have observed the thermal composite SNR Kes 27 with the ACIS-I detectors on *Chandra* and performed a spatially resolved spectroscopic study of the remnant. The main results are summarized as follows.

1. Superposed on the remnant, we have detected 30 point-like X-ray sources with $S/N \gtrsim 4$. Most are foreground stars, some are probably background AGN. None have the properties expected from a central compact stellar remnant. The upper limit to luminosity of a CCO or of a diffuse PWN is $\sim 1.5 \times 10^{32} \text{ ergs s}^{-1}$.
2. The X-ray spectrum of Kes 27 is characterized by K lines from ionized Mg, Si, S, Ar, and Ca. Most of the X-ray emitting regions are found to be sulphur-enriched. Calcium is also over-abundant in the remnant. The hot gas in the remnant is essentially close to ionization equilibrium (except for that along the eastern rim).
3. Images of the remnant show previously unseen double X-ray arc structures. There is an outer X-ray arc and an inner harder concentric arc. These two shell-like features are located in the northeastern half of the remnant and the X-ray surface brightness fades away with increasing radius in the south-west. The X-ray intensity peak coincides with the radio bright region along the eastern border. The gas in the inner region is at higher temperature.
4. The overall morphology can be explained by the evolution of the remnant in an ambient medium with density gradient increasing from west to the east. The remnant was probably born in a pre-existing cavity created by the progenitor star. The outer shock has hit the cavity wall and is now in the denser wall-material and the inner arc indicates gas heated by a reflected shock. This process may explain the X-ray morphology of this and even other thermal composite supernova remnants.

This work was supported by Chandra Grant GO3-4074X. Y.C. acknowledges support from NSFC grants 10725312, 10673003, and 10221001. F.D.S. thanks Scott Wolk for useful advice on star identification and Y.C. also

thanks Jasmina Lazendic and Pat Slane for previous collaboration on issues about reflected shock wave. We also thank an anonymous referee for helpful suggestions.

REFERENCES

- 2MASS Catalog, 2003, <http://www.ipac.caltech.edu/2mass/>
 Borkowski, K. J., Lierly, W. J., & Reynolds, S. P. 2001, *ApJ*, 548, 820
 Chen, Y., Su, Y., Slane, P. O., & Wang, Q. D. 2004, *ApJ*, 616, 885
 Cox, D. P., Shelton, R. L., Maciejewski, W., Smith, R. K., Plewa, T., Pawl, A., & Różyńska, M. 1999, *ApJ*, 524, 179
 Enoguchi, H., Tsunemi, H., Miyata, E., & Yoshita, K. 2002, *PASJ*, 54, 229
 Falle, S.A.E.G. 1981, *MNRAS*, 195, 1011
 Green, A. J., Frail, D. A., Goss, W. M., & Otrupcek, R. 1997, *AJ*, 114, 2058
 Harrus, I. M., Hughes, J. P., Singh, K. P., Koyama, K., & Asaoka, I. 1997, *ApJ*, 488, 781
 Helfand, D. J., Gotthelf, E. V. & Halpern, J. P., 2001, *ApJ*, 556, 380
 Hwang, U., Holt, S. S., & Petre, R. 2000, *ApJ*, 537, L119
 Kawasaki, M., Ozaki, M., Nagase, F., Inoue, H., & Petre, R. 2005, *ApJ*, 631, 935
 Kesteven, M. J. & Caswell, J. L. 1987, *A&A*, 183, 118
 Lazendic, J. S. & Slane, P. O. 2006, *ApJ*, 647, 350
 Leahy, D. 2004, *ApJ*, 127, 2277
 McClure-Griffiths, N. M., Green, A. J., Dickey, J. M., Gaensler, B. M., Haynes, R. F., & Wieringa, M. H. 2001, *ApJ*, 551, 394
 McKee, C. F. 1974, *ApJ*, 189, 17
 Milne, D. K., Caswell, J. L., Kesteven, M. J., Haynes, R. F., & Roger, R. S. 1989, *PASAu*, 8, 187
 Morrison, R., & McCammon, D., 1983, *ApJ*, 270, 119
 NED (National Extragalactic Database), 2007, <http://nedwww.ipac.caltech.edu/>
 Olbert, C. M., Clearfield, C. R., Williams, N. E., Keohane, J. W. & Frail, D. A., 2001, *ApJ*, 554, 205.
 Park, S., Roming, P. W. A., Hughes, J. P., Slane, P. O., Burrows, D. N., Garmire, G. P., & Nousek, J. A., 2002, *ApJ*, 564, L39
 Petruk, O. 2001, *A&A*, 371, 267
 Rho, J.H., & Petre, R. 1998, *ApJ*, 503, L167
 Reach, W. T., Rho, J., Tappe, A., Pannuti, T. G., Brogan, C. L., Churchwell, E. B., Meade, M. R., Babler, B., Indebetouw, R., & Whitney, B. A. 2006, *AJ*, 131, 1479
 Safi-Harb, S., Dubner, G., Petre, R., Holt, S. S., & Durouchoux, P. 2005, *ApJ*, 618, 321
 Sedov, L. I. 1959, *Similarity and Dimensional Methods in Mechanics* (New York: Academic)
 Seward, F.D., 1999, "Allen's Astrophysical Quantities", A. N. Cox editor, AIP Press, Chapter 9, 202.
 Seward, F. D., Kearns, K. E., & Rhode, K. L. 1996, *ApJ*, 471, 887
 Seward, F. D., Slane, P. O., Smith, R. K. & Sun, M., 2003, *ApJ*, 584, 414
 Sgro, A. G. 1975, *ApJ*, 197, 621
 Shelton, R. L., Cox, D. P., Maciejewski, W., Smith, R. K., Plewa, T., Pawl, A., & Różyńska, M. 1999, *ApJ*, 524, 192
 Shelton, R. L., Kuntz, K. D., & Petre, R. 2004, *ApJ*, 611, 906
 Slane, P., Smith, R. K., Hughes, J. P., Petre, R. 2002, *ApJ*, 564, 284
 Tokunga, A.T., 1999, "Allen's Astrophysical Quantities", A. N. Cox editor, AIP Press, Chapter 7, 151.
 USNO B1.0 Catalog, 2007, <http://www.nofs.navy.mil/data/fchpix/>
 Yusef-Zadeh, F., Wardle, M., Rho, J., & Sakano, M. 2003, *ApJ*, 585, 319
 Warren, J. S., Hughes, J. P., & Slane, P. O. 2003, *ApJ*, 583, 260
 Whiteoak, J. B. Z. & Green, A. J. 1996, *A&AS*, 118, 329